International Journal of Heat and Fluid Flow 74 (2018) 130–143

Contents lists available at ScienceDirect

International Journal of Heat and Fluid Flow

journal homepage: www.elsevier.com/locate/ijhff

An efficient micro-mixer by elastic instabilities of viscoelastic fluids: Mixing performance and mechanistic analysis

Cai Wei-Hua[1,*], Li Yong-Yao[1], Zhang Hong-Na[*], Li Yu-Ke, Cheng Jian-Ping, Li Xiao-Bin, Li Feng-Chen

School of Energy Science and Engineering, Harbin Institute of Technology, Harbin 150001, China

ARTICLE INFO

Keywords:
Mixing enhancement
Elastic instabilities
Viscoelastic fluids
Microchannel

ABSTRACT

Efficient mixing is one of the keen interest of many bioengineering and chemical engineering processes. In this work, we designed an efficient micro-mixer with viscoelastic fluid which can induce both strong shear and strong extension by being embedded several rhombic blocks to destabilize the viscoelastic fluid flow and can be also easily integrated. Experimental visualization and direct numerical simulation (DNS) of mixing process were conducted to evaluate the mixing performance. By adding green fluorescent particles into the fluids, apparent mixing enhancement was observed for viscoelastic fluid flow when the flow rate exceeded a threshold. The efficient micro mixing progress also shows great potential for bioengineering application with the biocompatible working fluids. Through DNS, we discussed the flow patterns and the role of polymers playing in viscoelastic fluid flow to respectively figure out the underlying mechanism of efficient mixing and the occurrence of unstable flow motions. The results show that when the elasticity is strong enough, the viscoelastic fluid flow is irregularly twisting and swinging in the channel, and as a result enhances the mixing by increasing the intersecting frequency of fluids of different concentrations. Moreover, owing to the special designed geometry, the polymers act as the energy supplier of unstable flow motions, which keeps the fluctuations from decaying towards the laminar regime.

1. Introduction

Recently, lab-on-a-chip (LOC) devices become an efficient and revolutionary solution to develop personal pharmacy, rapid diagnose of illness and materials synthesis (Ottino and Wiggins, 2004) and so forth. However, it faces a problem of poor mixing because of the encountered tiny dimension which confines the flow always being in laminar regime. In fact, efficient mixing is of great importance in many industrial processes, such as chemical engineering, biotechnology, *etc*. (Ng et al., 2015, Bhagat et al., 2005), that great mixing performance is beneficial to reduce the analysis time and the footprint of a lab-on-a-chip system. At macro scale, making flows to be chaotic and turbulent is one of the most effective manners to achieve an efficient mixing (Gan et al., 2007a), and the nonlinear inertia is the key to drive the flow to be turbulent when the Reynolds number (Re = UD/v, U: the characteristic velocity, D: the characteristic length, v: the kinematic viscosity of solution) is large enough. However, at micro scale, the nonlinear inertia is always too weak to induce the chaotic flow motions and only the molecular diffusion, which plays only at the interfaces between two different fluids, contributes to the mixing. Therefore, the mixing performance is often limited at this scale.

Seeking an efficient mixing manner at micro scale now attracts an increasing interest from lots of researchers working on microfluidics (Ammar et al., 2014; Li and Kim, 2017; Affanni and Chiorboli, 2010; McGovern et al., 2018; Ta et al., 2015; Stroock et al., 2002; Engler et al., 2003; Kockmann and Woias, 2003; Chen and Zhao, 2017; Akgönül et al., 2017; Mengeaud et al., 2002; Chen and Li, 2017; Mouheb et al., 2012; Haward et al., 2016a). With their efforts, various micro-mixers working either actively or passively have been designed. The common target of the existing micro-mixers is to induce unstable and chaotic flow motions no matter by active method or by passive method. In the active manner, some kinds of extra driving forces, typically pulsating pressure (Li and Kim, 2017), magnetohydrodynamic (MHD) (Affanni and Chiorboli, 2010) and ultrasonic (McGovern et al., 2018) forces *etc*., are introduced to disturb the flow. However, since the active ways often require the extra equipment and components, the

* Corresponding authors.
E-mail addresses: caiwh@hit.edu.cn (W.-H. Cai), yy-li@stu.hit.edu.cn (Y.-Y. Li), zhanghn@hit.edu.cn (H.-N. Zhang), liyuke_lyric@hotmail.com (Y.-K. Li), chjp@hit.edu.cn (J.-P. Cheng), lixb@hit.edu.cn (X.-B. Li), lifch@hit.edu.cn (F.-C. Li).
[1] The authors contributed equally to this paper.

https://doi.org/10.1016/j.ijheatfluidflow.2018.09.006
Received 14 April 2018; Received in revised form 9 August 2018; Accepted 14 September 2018
0142-727X/ © 2018 Elsevier Inc. All rights reserved.

Nomenclature

c	concentration
$\mathbf{C}$	conformation tensor
D	characteristic length
D_d	diffusion coefficient of the fluids
De	Deborah number
D_k	generalized diffusion term of the instantaneous kinetic energy
E_r	relative error between the numerical results and experimental ones
E_a	absolute error between the numerical results and experimental ones
E_k	instantaneous kinetic energy
E_{kf}	turbulent kinetic energy
E_p	instantaneous elastic energy
F_k	energy input by the external force
G_p	energy exchange between the flow motion and the polymers
G_p'	elastic contribution to the turbulent fluctuations
h	channel height
p	fluid pressure
Q_{in}	flow rate of the middle inlet
Re	Reynolds number
Sc	Schmidt number
t	time
U	characteristic velocity
$\mathbf{u}$	velocity field
u_{in}	velocity at the middle inlet
w	width of the inlet channel
Wi	Weissenberg number
ν	kinematic viscosity
μ	dynamic viscosity
λ	relaxation time of viscoelastic fluid
ρ	density of fluid
η_o	total viscosity
η_s	solvent dynamic viscosity
η_p	solute dynamic viscosity
η_{EM}	mixing efficiency
η_{Num}	efficiency of numerical results
η_{Exp}	efficiency of experimetal results
$\boldsymbol{\tau}$	stress tensor
$\boldsymbol{\tau}_s$	solvent contribution to the stress tensor
$\boldsymbol{\tau}_p$	solute contribution to the stress tensor
β	ratio of solvent viscosity to total viscosity
ε_v	viscous dissipation of the mean kinetic energy

mixing system of this kind is expensive and difficult to be integrated. On the other hand, the passive method enhances the mixing through modifying the geometrical configurations, such as embedding T-shaped structures, complex three-dimensional (3D) structures and two-dimensional (2D) or planar structures *etc*., into the micro-mixers to excite unstable and chaotic flows (Ta et al., 2015). Comparing with the active way, the method of this kind is easier and cheaper for system integration in the diagnose devices and micro reaction devices. Among them, complex 3D micro-mixers, which are made up of channels layer-by-layer, can work efficiently at relatively lower *Re* (Stroock et al., 2002) but at the cost of fabrication manipulate. Comparing with 3D micro-mixers, planar micro-mixers, such as T-shaped micro-mixers (Engler et al., 2003; Kockmann and Woias, 2003; Chen and Zhao, 2017), curved microchannel (Akgönül et al., 2017), zig-zag micro-mixers (Mengeaud et al., 2002; Chen and Li, 2017), cross-slot geometry (Mouheb et al., 2012; Haward et al., 2016a) and rhombic micro-mixer (Chung and Shih, 2008), are much simpler for fabrication, but usually require high-Re operating conditions, namely high-pressure drop. As aforementioned, the key of the micro-mixers is to induce unstable and chaotic flow motions at low Re. Changing the working medium, such as adopting non-Newtonian fluid, is an efficient way to reach this target.

Viscoelastic fluids, a typical type of non-Newtonian fluids, *e.g.*, solutions of some flexible high-molecular-weight polymers or surfactants, widely exists in nature. Different from Newtonian fluid flow, an additional nonlinear elastic effect, originating from long-chain polymers or flexible microstructures, exist besides the nonlinear inertial effect. The strength of elastic nonlinearity is often described by Weissenberg number ($\text{Wi} = \lambda U/D$, λ: the relaxation time of fluids) or Deborah number ($\text{De} = \lambda/\tau$, τ: the characteristic time of flow). Since Wi is inversely proportional to the channel dimension, the existence of elastic nonlinearity in viscoelastic fluid flow provides us another chance to excite chaotic flow motions at micro scale where inertia nonlinearity can be ignored but the elastic nonlinearity can solely dominate the flow. When Wi is above a critical value, the nonlinear elasticity can solely induce the flow transition from a laminar regime to a turbulent status which is the so-called elastic turbulence. The flow of this regime has been experimentally observed in several geometries, such as parallel-disk (Groisman and Steinberg, 2000; Burghelea et al., 2007), cone-and-disk (Groisman and Steinberg, 2004), Taylor-Couette (Akgönül et al., 2017), serpentine microchannels (Burghelea et al., 2004; Jun and Steinberg, 2011; Li et al., 2016b; Feng-Chen et al., 2012b; Li et al., 2016a), channel with cylindrical obstacles (Li et al., 2010), *etc*. Therein, the flow shows some features of developed inertial turbulence, *e.g.*, an abrupt increase of flow resistance, turbulent fluctuations of a wide range of temporal and spatial scales, turbulent structures of intermittency, and so forth. Recalling the common target of micro-mixers, this phenomenon shows a great potential to enhance mixing and heat transfer at micro scale. Currently, the mixing enhancement by this flow motion has been demonstrated by Groisman and Steinber (2001), Pathak et al. (2004) and Haward et al. (2016a) in a curvy microchannel. In their studies, the geometrical curvature plays as a trigger of elastic instabilities and elastic turbulence. Haward et al. (2016a) and Li et al. (2014) made an in-depth discussion on the mechanism of mixing enhancement by elastic instabilities from viewpoints of vortex structures and scalar transports. In addition to the above curvy microchannels, recently, both numerical and experimental measurements showed the occurrence of purely elastic instabilities in straight microchannels (Zhang et al., 2013; Pan et al., 2013; Bonn et al., 2011). Therein, the microchannels are specially designed either with large perturbation generator such as placing several cylinder obstacles at inlet or with nontrivial structures such as symmetrically and staggeredly adding 'well' structures to the sidewall of straight channel. However, without the initial or instantly generated perturbations, the straight wall tends to stabilize the elastic turbulent flow (Zhang et al., 2016; Hong et al., 2016; Julius et al., 2016). It is notable that in above microchannels, the key to induce the elastic instabilities lies in the shear flows. In fact, except the shear flows, the extension-dominated flow including flows through contractions and expansions and intersections (like cross slot, T- or Y-shaped junctions) can also trigger the elastic instabilities, *i.e.*, the so-called extensional elastic instabilities. In contraction-expansion geometry, the flow experiences a positive streamwise velocity gradient as it entering the contraction and a negative streamwise velocity gradient through the expansion (Groisman and Steinberg, 2004; Burghelea et al., 2004; Jun and Steinberg, 2011; Li et al., 2016b; Feng-Chen et al., 2012b). When the viscoelastic fluid passing a channel of this type, the recirculating vortices in the abrupt contraction/expansion microchannels appear asymmetrically when De exceeds a threshold. The unstable flow motions in this channel have

been well documented (Gan et al., 2006; Lam et al., 2009; Gan et al., 2007b). In addition to the flow in contraction-expansion geometry, the stagnation-point flow, such as the flow through the cross slot (Haward et al., 2016b,2012) or T- or Y- shape channel (Soulages et al., 2009; Squires and Quake, 2005) is another classical extensional flow with a stagnation point in the intersection point of two opposite branches. Again, when the elasticity dominates the flow, the extensional elastic instabilities occur acting as the bi-stable flow motions or the time-dependent oscillating flow motions around the stagnation points (Poole et al., 2007). The stagnation-point flows of viscoelastic fluids have been recently reviewed by Haward (2016). The extensional elastic instabilities especially in the stagnation point-flow show the ability to enhance the mixing at micro scale Galindo-Rosales et al. (2013). However, the mixing in the above-mentioned microchannels is not efficient enough due to the single stagnation point encountered and the throughput is limited by the difficulties of integration and parallel running due to the existence of multiple branches. Therefore, the application of extensional elastic instabilities to promote the mixing is still very limited and a suitable channel design is required.

In sum, the unstable viscoelastic fluid flow motions can be excited in the above-mentioned microchannel of various geometries via either shear or extension dominated flows. However, as a micro-mixer, most of the aforementioned geometries, like curvy channel, cross slot as well as T-shaped channel, is difficult to be integrated. In this paper, we designed a new 2-D planar microchannel, which can achieve an efficient mixing performance and be easily fabricated and integrated, where both strong shear and strong extension are induced to destabilize the viscoelastic fluid flow. Experimental visualization and direct numerical simulation (DNS) are conducted to investigate the performance of this mico-mixer. To clarify the essence of the mixing enhancement and the elastic instability in this channel, the flow characteristics, the mixing process and the energy balance between the flow motion and the polymers are then discussed. The rest paper is organized as follows: Section 2 introduces the micro-mixer we designed, and presents the experimental evidence of better mixing performance of viscoelastic fluid flow in the current micro-mixer; Section 3 is developed for DNS and presents the governing equations used in the following sections; the numerical results are then discussed in detail in Section 4; finally, Section 5 draws the conclusions of the present paper.

2. Design of the micro-mixer

As introduced above, the shear flows and the extensional flows, typically existing in the turning and intersecting positions of T- or Y-shaped channel respectively, can induce elastic instabilities under creeping flow conditions. Here, we propose a micro-mixer with several rhombic blocks as shown in Fig. 1(a), which contains continuous confluences and shunting along the flow direction, and perfectly satisfies the requirements (shear dominating before confluences, while extension dominating in the junctions) to induce two typical elastic instabilities. It has three inlets, six rhombic structures and an outlet in the end of the channel with the channel height h of 50 μm. The included angle of side-inlets and middle inlet channel is 45°, and the side channels share a half width of the middle one w which is 200 μm. Moreover, the six-rhombic-channel which is the core of the mixing channel and shares only the length of 3400 μm, located at 2 cm downstream from the start of the straight channel. Unlike the existing micro-mixers, this one is distinct not only for the elastic instability induced by coupling shear and extensional flows, but also for the integrating convenience. Fig. 1(b) shows a schematic of the channel integration, and hereby, the junction number can increase easily to run parallel with no need to excessively extend the channel length.

The microfluidic channel was fabricated by the soft lithography techniques using PDMS-glass compounded layer. The fabrication process begins with a negative transparent photomask (800V2, Creo) printed at a resolution of 2540 dpi containing the design of

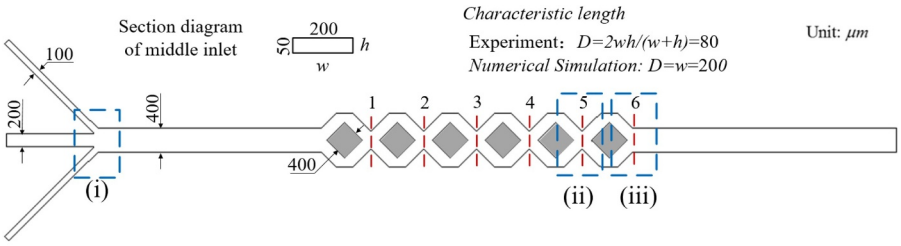

(a)

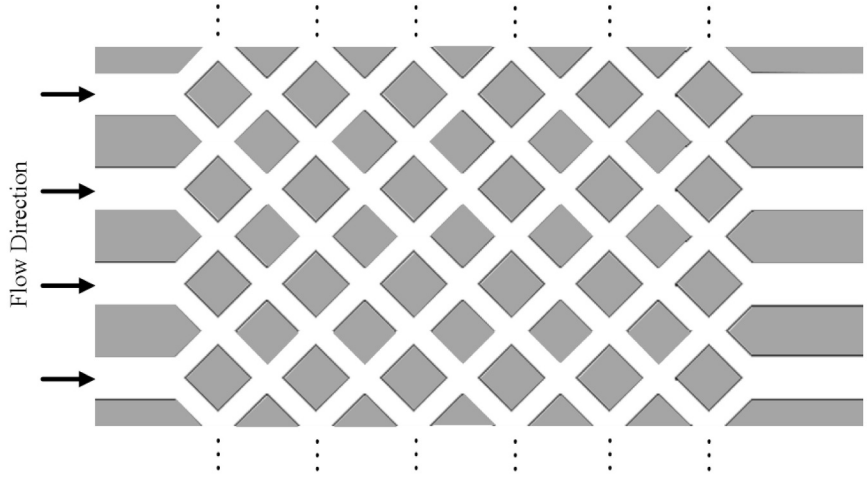

(b)

Fig. 1. Schematics of (a) the micromixer with rhombic structures and (b) the channel integration. The blue boxes indicate the windows in the experimental visualization and the dashed lines 1 to 6 indicate 6 monitor positions in DNS. (For interpretation of the references to color in this figure legend, the reader is referred to the web version of this article.)

microchannel drawn in AutoCAD in advance. A 50-μm thick dry film (FX250, DuPontTM Riston) was coated on a clean stainless steel plate mirror-polished and exposed under a 380 nm UV LED (TH-UV380S10X-5, Tianhui) array for 45 min. Then, a positive master copy on the stainless steel plate was obtained by washing away the unexposed photoresist in a developer solution (1% wt dilute Na_2CO_3 aqueous solution). Liquid PDMS was prepared by mixing pre-polymer based (Sylgard, Dow Corning) with the curing agent by the weight ratio of 10:1. Once both liquid components are thoroughly cross-linked, the mixture was poured onto the previous fabricated mold. In order to reduce the curing time of PDMS, the positive mold was placed into a vacuum oven (RVD-300, As-one) for 20 min' de-airing and heated in a high temperature chamber (DZF, Bluepard) at 80 °C for 60 min. After the PDMS was peeled off from the channel mold by a lancet, several holes were punched through the PDMS slab according to the reserved circles in the microchannel serving as reservoirs of inlets and outlets.

Rheological properties of the working fluids including dynamic viscosity and relaxation time were measured at 25 °C by a rotational rheometer (Kinexus Pro, Malvern instruments, UK). The rheometer used a concentric system with a Peltier cylinder cartridge of which the inner and outer diameters are 25 mm and 27.5 mm, respectively, and the height is 40 mm. As an example of Newtonian fluid, we used sucrose solution (45% wt.) whose dynamic viscosity μ is 0.00945 Pa·s and density ρ is 1200.4 kg/m^3. As an example of viscoelastic fluid, we used an aqueous solution with 10% polyethylene glycol (PEG; MW = 8000; Sigma-Aldrich) and 0.1% polyethylene oxide (PEO; MW = 2×10^6; Sigma-Aldrich) which is a typical Boger fluid with the dynamic viscosity μ of 0.01094 Pa·s for shear rate between 1 and 360 s^{-1} (as shown in Fig. 2(a)) and the density ρ of 1204.8 kg/m^3. Fig. 2(b) shows the linear viscoelastic measurements of the angular-frequency (ω)-dependent complex shear modulus. The relaxation time of the polymer chains is estimated by the frequency ω_c which located at the intersection points of G′ and G″. As shown in Fig. 2(b), the frequency ω_c is 120 rad/s and thus the relaxation time λ ($\lambda = 2\pi/\omega_c$) is 0.052 s. Table 1 listed the rheological properties of working fluids and experimental cases involved in the present work. The flow rate Q_{in} in the middle inlet ranges from 0 to 20 μl/min under which the maximum Re ($Re = \rho u_{in} D/\mu$, where u_{in}: the mean velocity at the middle inlet, $u_{in} = Q_{in}/(hw)$) for Newtonian fluid flow and viscoelastic fluid flow are 0.339 and 0.295 respectively and the maximum Wi ($Wi = \lambda u_{in}/D$) is 21.667 for viscoelastic fluid flow.

The micro-mixer performance was then experimentally visualized to evaluate its mixing performance. The solution with green fluorescent particles (Thermo Sci., 0.92 μm) was injected in the middle inlet while the fluoresce-free solution was injected from the side inlets. Two syringe pumps were used to ensure the total flow rate the same for two kinds of solutions. The mixing process was tracked continuously by an inverted microscope (IX71, Olympus) with a CMOS camera at rate of 5000 frames per second and 190 μs exposure time per frame. We mainly keep eyes on three regions which are near the inlet, the middle region and near the outlet as marked by blue frames in Fig. 1(a). Fig. 3(a) illustrates the comparison of mixing performance between Newtonian fluid flow and viscoelastic fluid flow. For brevity, the Newtonian fluid flow case with the maximum Re_{in} is only shown owing to the same tendency when varying Re_{in}. It is obvious that because of low Re the Newtonian fluid flow stays laminar in the whole channel so that the mixing barely occurs with the fluorescently-labeled flow staying in line in the center of the micro-mixer. Viscoelastic fluid flow is also stable when Wi is extremely small. By gradually increasing Wi, flow instability (elastic instability) start to occur when Wi is larger than critical Wi (V2 case in the present work). In this case, faint mist appears in the path of fluorescence-free solution, indicating that the fluorescently-labeled flow invades into the fluorescence-free ones and the occurrence of the unstable flow and the slight convection being at play as shown in the white dashed box in Fig. 3. However, the mixing is still inefficient under this condition since the instability or the convection is not strong enough. Further increasing Wi, the fluorescently-labeled flow solution spans among the whole channel rapidly and becomes almost uniform after passing several rhombic structures when Wi is 21.667. From the animation (see the supplementary Video 1 to Video 3), it is clearly seen that comparing with the Newtonian fluid flow, in viscoelastic fluid flow the twisting flow motions exist and continuously intake the fluorescently-labeled solution to the fluorescence-free ones in the rhombic channel, which is the key to enhance the mixing.

Moreover, it is interesting to notice that the slight swinging motions start in the straight channel before entering the first rhombic structure, which acts as the asymmetrical distribution of the fluorescence-free fluid just after the junction of three inlets (as shown in supplementary video 3). Fig. 3(b) illustrates the flow of V3 case at the entrance of the first rhombic channel. It is obvious that the fluid with fluorescence particles occupy a wider area of the channel indicating that it diffuses horizontally during the straight channel after the inlet junction. It is the result of the unstable flow in the straight channel which is caused by the extensional flow (Arratia et al., 2006) at the junction of inlets-channel. In other words, this inlet design also promotes the occurrence of

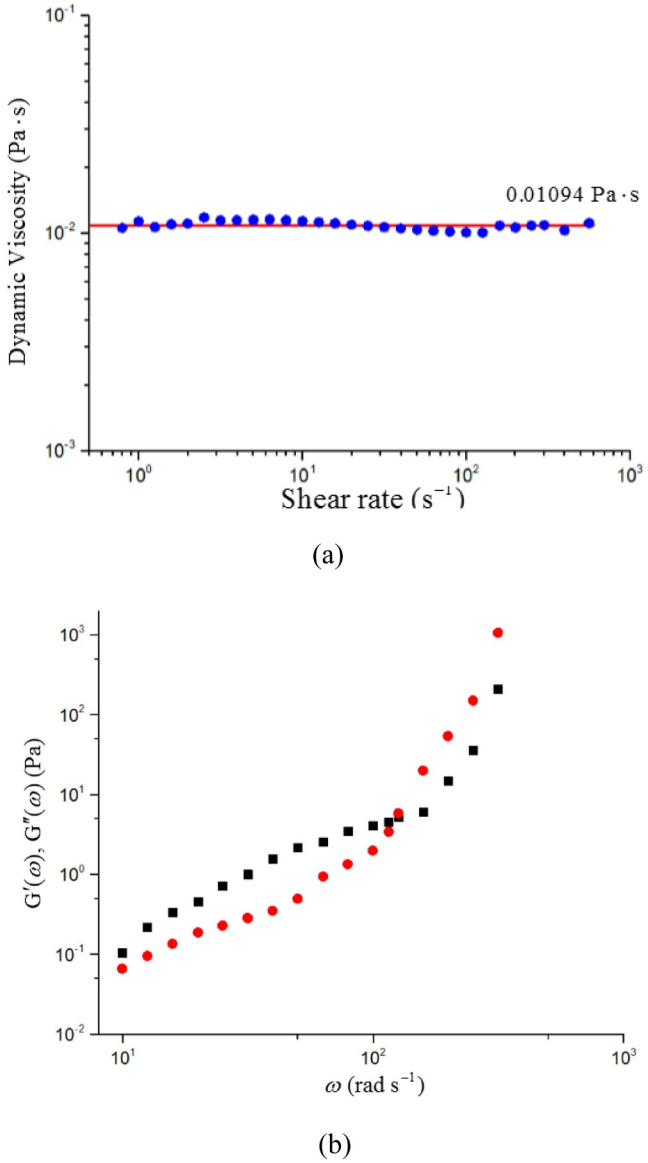

Fig. 2. Rheological properties of viscoelastic fluid in the present work: (a) dynamic viscosity at different shear rates;(b) oscillatory shear rheology of viscoelastic fluid.

Table 1
Rheological properties of working fluids and experimental cases involved in the present work.

Experimental conditions	Dynamic viscosity (Pa·s)	Relaxation time (s)	Flow rate (μl/min)	Re	Wi
Newtonian case (N)	0.00945	0	20	0.339	0
Viscoelastic case 1 (V1)	0.0109	0.052	1	0.015	1.083
Viscoelastic case 2 (V2)	0.0109	0.052	5	0.073	5.417
Viscoelastic case 3 (V3)	0.0109	0.052	20	0.295	21.667

unstable flow motions in viscoelastic fluid flow. Hence, before entering the rhombic structures, the mixing performance of viscoelastic fluid flow is relatively better than that of Newtonian fluid. However, the flow instability is not sustained downstream so that the flow instability in the extensional flow region does not greatly increase the mixing efficiency in the straight channel. So the rhombic channel plays great role in maintaining the flow instability for mixing enhancement.

The mixing efficiency is then quantified by η_{EM} ($\eta_{EM} = 1 - \frac{\sigma}{\bar{I}}$), where σ is the standard deviation of the intensity and $\bar{I}$ is the average value of an intensity distribution. For each condition, an averaged grayscale image was firstly obtained for 200 recorded color images of the outlet zones as marked in blue frame (iii) in Fig. 1(a). It should be noted that we took a measurement 30 sec after started the flow to ensure a stable flow rate in the channel, although the instable flow at high Wi happens rapidly when we applied a high flow rate in the experiment. Fig. 4 shows the averaged outlet intensity distribution and η_{EM} for each case. It is clearly seen that the viscoelastic fluid flow at higher Wi (V3 case) has much better mixing performance than those of Newtonian fluid flow and lower Wi-number viscoelastic fluid flows (V1 and V2 cases). The η_{EM} for viscoelastic fluid flow at Wi = 21.667 reaches near 86.15%, which is more than twice of that for the Newtonian fluid flow under similar Re. And mixing progress is not only efficient but also relatively fast that achieving such a good mixing performance, the mixing time is only about 0.1 s. Also, the working fluids, the Boger fluid with PEG and PEO, is biocompatibility so that such a mixing progress in the designed micromixer shows potential for bioengineering. In sum, the visualization and the quantification of the mixing performance confirmed the ability of mixing enhancement by viscoelastic fluids in the designed micro-mixer.

However, limited by the current experimental techniques, it is difficult to gain further insight into the mixing process, such as the flow patterns, the polymers' deformation, especially the role of polymers and so forth, which are necessary to understand the underlying mechanism of mixing enhancement. In this sense, the numerical solution can provide the more detailed information as a compensation, which is the focus of next section.

3. Numerical procedures

DNSs of mixing process of Newtonian fluid and viscoelastic fluid flows in the 2D planner microchannel were carried out on the open source software OpenFOAM (Favero et al., 2010), which is based on the collocated finite-volume method (FVM) and has been proven to be an adequate choice of platform for analysis of viscoelastic fluid flow (Habla et al., 2014). The dimensionless governing equations were solved to make the computational results more universal. To deal with the numerical breakdown at high Wi, the newly developed module in terms of the log-conformation reformulation (LCR) (Fattal and Kupferman, 2004) is employed. This module has been validated in our previous work by several benchmarks, such as the creeping flows of viscoelastic fluids around a confined cylinder, the details of which can be found in Refs. (Li et al., 2017; Zhang et al., 2017). In this work, we developed a specific solver for the mixing problem of viscoelastic fluids by introducing the above-mentioned module.

3.1. Governing equations

Considering viscoelastic fluid flow to be incompressible, based on the continuum hypothesis, the mass and momentum conservation equations are shown respectively as

$$\nabla\cdot\mathbf{u} = 0 \tag{1}$$

$$\frac{\partial\mathbf{u}}{\partial t} + \mathbf{u}\cdot\nabla\mathbf{u} = -\frac{1}{\rho}\nabla p + \frac{1}{\rho}\nabla\cdot\tau \tag{2}$$

where $\mathbf{u}$ is the velocity field; ρ denote the density of fluid respectively; t is time; p is fluid pressure; $\boldsymbol{\tau}$ is the stress tensor consisting of both solvent and elastic solute contributions as

$$\tau = \tau_s + \tau_p \tag{3}$$

Therein, the solvent contribution $\boldsymbol{\tau}_s$ is defined by

$$\tau_s = \eta_s[\nabla\mathbf{u} + (\nabla\mathbf{u})^T] \tag{4}$$

where η_s is the solvent dynamic viscosity. The solute contribution $\boldsymbol{\tau}_p$ can be expressed by certain constitutive model according to the type of viscoelastic fluid. This work adopts Oldroyd-B model which describes the main properties of Boger fluids and is presented as

$$\tau_p + \lambda\left[\frac{\partial\tau_p}{\partial t} + \nabla\cdot(\mathbf{u}\tau_p) - (\nabla\mathbf{u})^T\cdot\tau_p - \tau_p\cdot(\nabla\mathbf{u})\right] = \eta_p[\nabla\mathbf{u} + (\nabla\mathbf{u})^T] \tag{5}$$

where λ is relaxation time of viscoelastic fluid and η_p is the solute dynamic viscosity.

In terms of conformation tensor, the constitutive relation of Oldroyd-B model is defined as

$$\tau_p = \frac{\eta_p}{\lambda}(\mathbf{C} - \mathbf{I}) \tag{6}$$

where $\mathbf{C}$ denotes the conformation tensor and is a symmetric tensor; $\mathbf{I}$ is the unit tensor. Substituting Eq. (6) into Eq. (5), Eq. (5) can be rewritten in the form of conformation tensor as

$$\frac{\partial\mathbf{C}}{\partial t} + \mathbf{u}\nabla\cdot\mathbf{C} - (\nabla\mathbf{u})^T\cdot\mathbf{C} - \mathbf{C}\cdot(\nabla\mathbf{u}) = \frac{1}{\lambda}(\mathbf{I} - \mathbf{C}) \tag{7}$$

Moreover, in order to gain more universal computational results, the dimensionless governing equations are used based on the following dimensionless criteria: $\nabla^+ = D\cdot\nabla$, $\mathbf{u}^+ = (u_x, u_y, u_z)/u_{in}$, $t^+ = t\cdot u_{in}/D$, and $p^+ = p/(\rho\cdot u^2_{in})$, where D is the Characteristic length of microchannel; u_{in} is the maximum inlet velocity in the flow direction. The dimensionless governing equations are shown as follows:

$$\nabla^+\cdot\mathbf{u}^+ = 0 \tag{8}$$

$$\frac{\partial\mathbf{u}^+}{\partial t} + \mathbf{u}^+\cdot\nabla^+\mathbf{u}^+ = -\nabla^+p^+ + \frac{\beta}{Re}\nabla^{+2}\mathbf{u}^+ + \frac{(1-\beta)}{Re\cdot Wi}\nabla^+\cdot\mathbf{C} \tag{9}$$

$$\frac{\partial\mathbf{C}}{\partial t^+} + \mathbf{u}^+\nabla^+\cdot\mathbf{C} - (\nabla\mathbf{u}^+)^T\cdot\mathbf{C} - \mathbf{C}\cdot(\nabla^+\mathbf{u}^+) = \frac{1}{Wi}(\mathbf{I} - \mathbf{C}) \tag{10}$$

$$\frac{\partial c}{\partial t^+} + \mathbf{u}^+\cdot\nabla^+c = \frac{1}{Re\cdot Sc}\nabla^{+2}c \tag{11}$$

where, $Re = u_{in}\cdot D/\eta_o$, $Wi = \lambda\cdot u_{in}/D$ and $Sc = \eta_o/D_d$ are the Reynolds number and Weissenberg number as well as Schmidt number, respectively; D_d is the diffusion coefficient of the fluids; β is the ratio of solvent viscosity to total viscosity η_o ($\eta_o = \eta_s + \eta_p$), defined as $\beta = \eta_s/(\eta_s + \eta_p)$; c is the concentration which ranges from 0 to 1.

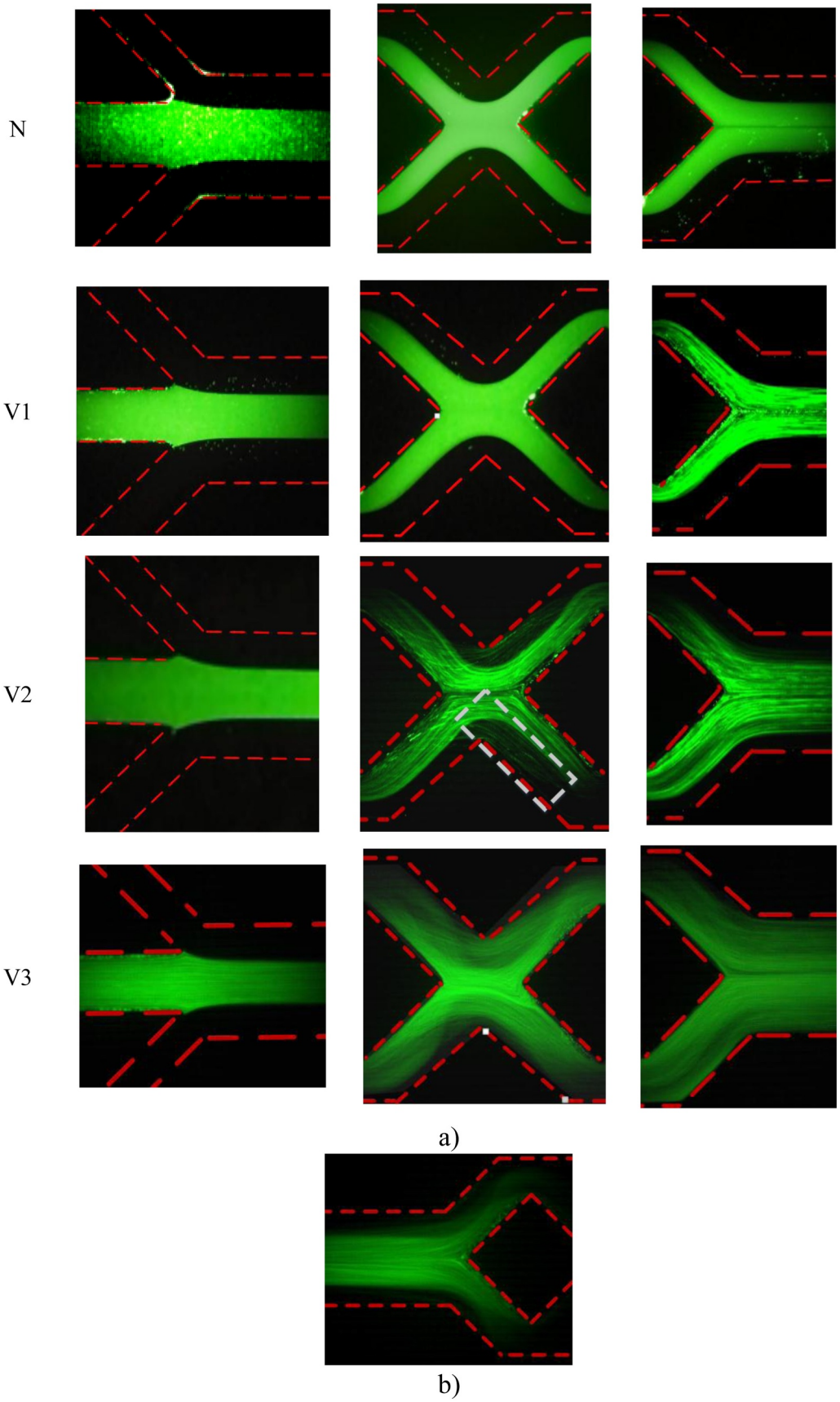

Fig. 3. Mixing performance of Newtonian fluid flow and viscoelastic fluid flows: a) comparison of mixing performance between Newtonian fluid flow and viscoelastic fluid flow; b) flow of V3 case at the entrance of the first rhombic channel.

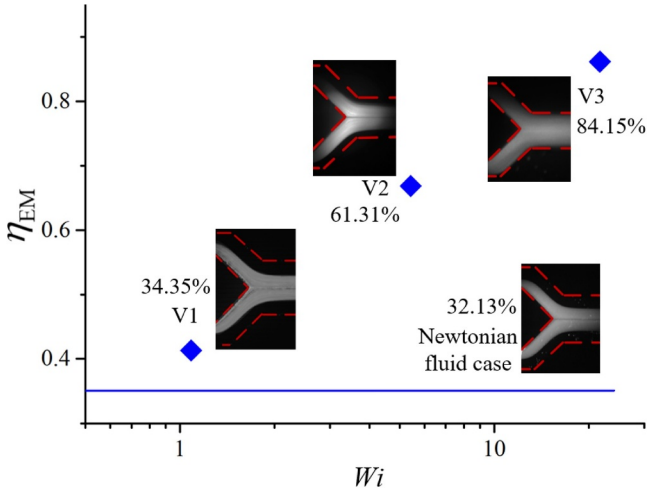

Fig. 4. The images of averaged outlet intensity distribution and mixing efficiency of each experimental case.

3.2. Boundary conditions and numerical schemes

The numerical geometry is similar to that used in experiments as illustrated in Fig. 1(a) except in two dimension (2D) because of the consuming computational memory of 3D simulation of viscoelastic fluid flow in this complex geometry. Nevertheless, the 2D numerical results showed quite similar flow features and mixing efficiency (see details in Section 4.1) as those observed in experiments, thus they are very helpful to understand the mechanism of mixing enhancement and elastic instability especially the polymers deformation.

During the simulation, the mean dimensionless velocity was set to be 1.0 in the middle inlet and 1.0 in the side ones to ensure the same flow rate of the two different fluids while dimensionless zero pressure was set in the outlet corresponding to natural outflow condition. For the mixing process, the concentration c was set to be 1.0 in the middle inlet while 0 in both side ones. Besides, the conformation tensor $\mathbf{C}$ was set to be a unit tensor in the inlet, namely long-chain molecules being in the coiled status, and to have zero gradient in the outlet and on the wall.

As for the numerical discretization, the first-order Euler implicit scheme was used for time marching in the unsteady transport equations of Eqs. (9)–(11) with the small dimensionless time step $\delta_t = 10^{-3}$. The convection terms were discretized by QUICK scheme for momentum conservation equation, while bounded MINMOD scheme for the concentration transport equation and conformation tensor transport equation. What's more, the mixing process of viscoelastic fluid flow at Re = 1, Wi = 20, which has the highest Wi among all the numerical cases, was simulated based on different grid resolution to get a grid independent solution. Fig. 5 shows the obtained η_{EM} for different grids. With the increase of the grid number, η_{EM} decreases and reaches convergent. Considering both the accuracy and the efficiency of the simulation, we adopted the grid with 52,230 nodes. Moreover, all the simulations last for more than $400D/u_{in}$ as shown in Fig. 6 to achieve a statistical steady status and enough data for the statistical analysis in the following sections.

4. Numerical results and discussions

All the numerical conditions in this work are listed in Table 2. This section mainly analyzes the flow features and the mixing performance of both Newtonian fluid and viscoelastic fluid flows in the micro-mixer obtained through 2D DNS. The mixing performance is firstly evaluated by the contours of concentration field intuitively and the quantification of mixing efficiency. Also, in order to be convincing, the DNS results about mixing performance are compared with experimental results in familiar cases. The flow patterns and the role of elastic stress are then analyzed to understand the mixing performance from the viewpoints of respectively the flow field and the elasticity feedback.

4.1. Performance of viscoelastic micro-mixer

Fig. 7 shows the contours of the time-averaged concentration field after the simulation reaching statistical steady status (as shown in Fig. 6) in the microchannel for different fluids. As the flow rate of the middle inlet equals to the total flow rate in the upper and the lower inlets, c should be 0.5 represented by green color if the coming liquids are perfectly mixed. As demonstrated in Fig. 7, the mixing process is obviously different for Newtonian fluid and viscoelastic fluid flows. Through the whole channel, Newtonian fluids (Re = 1, Wi = 0) are barely mixed with a stratified and symmetric concentration distribution in the lateral direction. However, when it comes to the viscoelastic fluid cases, the mixing at the end of the rhombic channel is prominent comparing with that in Newtonian fluid case. To understand the origin of different mixing performance, we then analyzed the mixing process through the whole channel in detail. From the temporal evolution of the concentration field (see the supplementary Video 4 to Video 6), it was seen that the fluids with different concentrations in viscoelastic fluid cases mixed frequently with the irregularly waving and rolling flow motions during the straight and rhombic channel, and as a result the distribution of concentration field in viscoelastic fluid flow becomes uniform (approximate 0.5) rapidly in the first few rhombic structures when Wi is large enough (Wi > 1). Moreover, for the high-Wi cases (Wi > 1), the mixing in viscoelastic fluid cases start to occur from the junction of three inlets which also promotes the mixing in the straight channel before entering the rhombic channel while the flow stay layered for Newtonian fluid case and low-Wi viscoelastic fluid cases (Wi < 1). The occurrence of viscoelastic flow instability at the junction of three inlets is also observed by our experiment and previous research (Hong et al., 2016). Consequently, the mixing length for the viscoelastic fluid cases is much shorter than that required for Newtonian fluid flow under the low-Re flow condition. In addition, it is also seen that under the same Re (Re = 1) increasing Wi shortens the mixing length for a certain range of Wi, while the mixing saturates when Wi is above 5. At the same Wi (Wi = 5), increasing Re slows down the mixing and extends the mixing length required as shown in Fig. 7(b). The above qualitative observation is similar to that in the experimental visualization.

Similar to that in Section 3, the mixing efficiency η_{EM} was also calculated based on the numerical results, where σ is the standard deviation of the concentration and $\bar{I}$ is the average value of the

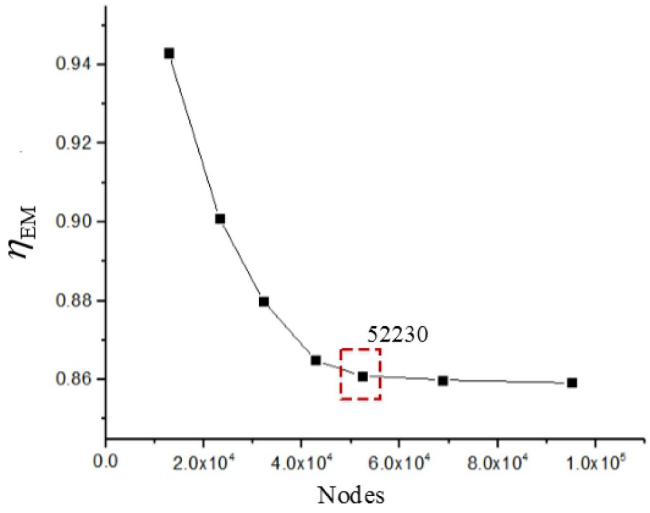

Fig. 5. Grid independency.

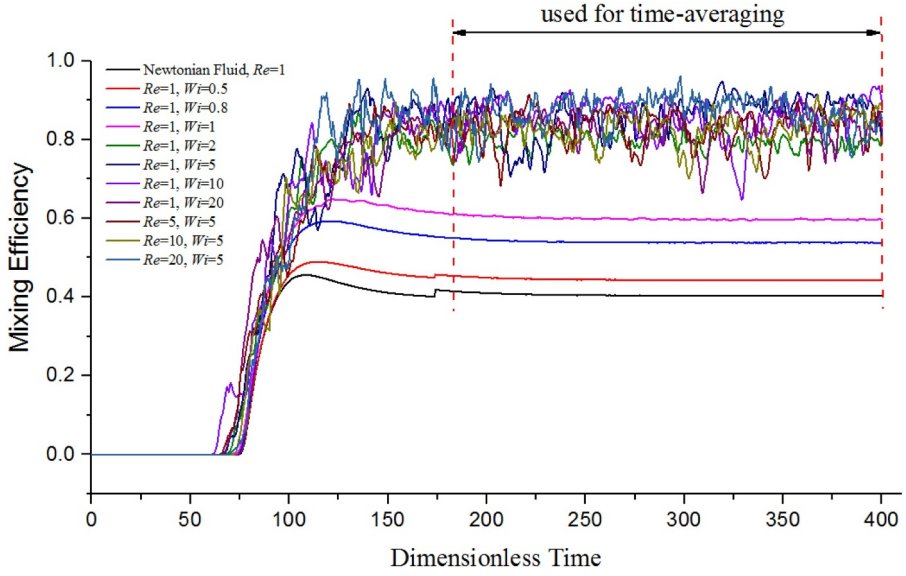

Fig. 6. Temporal evolution of mixing efficiency in different cases.

Table 2
Numerical conditions in the present work.

Cases	δ_t	Re	Wi	β	Sc
Newtonian fluid case	10^{-3}	1	0	1	
Viscoelastic fluid cases	10^{-3}	1	0, 1, 2, 5, 10, 20	0.9	1×10^8
		1, 5, 10, 20	5		

concentration distribution and is 0.5 corresponding to the expected concentration after perfectly mixing.

Fig. 8 illustrates the time-averaged η_{EM} at six different lines (as shown in Fig. 1(a)) under different flow conditions. Focusing on their final mixing performance, it can be observed that comparing with Newtonian fluid flow, there exists a dramatic increase of mixing efficiency for viscoelastic fluid flow when Wi increases to a critical value of $O(1)$ at the same Re (Re = 1). As Wi increases above 5, the mixing performance reaches a saturated status with η_{EM} (89.1%) almost twice as that of Newtonian fluid flow (38.4%), which agrees well with that in the experimental results. This quantitatively proves the efficient mixing for larger Wi. Moreover, since the molecular diffusion dominates the mixing in Newtonian fluid flow, the mixing performance improves linearly with the distance from the inlet as shown in Fig. 8(a). Looking at viscoelastic fluid flows, the mixing rate accelerates in the first few rhombic structures with increasing Wi as demonstrated by the larger slope in viscoelastic fluid cases in Fig. 8(a), and then slowdown in the last few rhombic structures because the mixing rapidly reaches a saturated status. At the first monitoring position, the mixing performance for low-Wi cases (Wi = 0.5, 0.8 and 1) is close to that in Newtonian fluid case, while it is improved significantly for high-Wi cases (Wi > 5) because the junction of three inlets can also promote the mixing before entering the rhombic structures, as demonstrated in supplementary video 5 and video 6 by numerical simulation and video 3 by experimental visualization. In consistence with Fig. 8(b), for the same Wi, the mixing is weakened by a higher Re, implying the attenuating effect of inertia on the induction of elastic instabilities. Since Re is so low that the inertia is very weak and plays an attenuating effect, we reached a conclusion that the elastic effect in viscoelastic fluid flow is solely responsible for the observed mixing enhancement.

4.2. Mechanistic analysis on the mixing enhancement

The above analysis of both experimental visualization and numerical results concludes the high mixing efficiency of viscoelastic fluid flow at low Re in the proposed rhombic microchannel. To gain further insight into the mixing enhancement, this section focuses on the instantaneous flow field.

Before the further analyzes, it should be notice that in this work, we adopt 2D simulation which will bring a certain error for lacking consider parts of viscous effect caused by walls. However, when Wi exceeds the critical Wi, elastic effect dominates the flow, so that the influence of viscous effect is weak in the elastic unstable flow. To this end, 2D simulation results are reliable in high-Wi condition. Also, as shown in our work, the quantitative result and the phenomena of 2D numerical simulation agree the experiment result very well at high Wi. Additionally, we think it may be an efficient way to adopt 2D simulation for designing the micromixer which is based on the unstable flow.

Fig. 9 shows the contours representing the temporal evolutions of concentration field for Newtonian fluid and viscoelastic fluid flows, where t indicates the dimensionless computational time. It is seen that the concentration distribution of Newtonian fluid flow is kept in a stratified status with the temporal evolution. In contrast, the mixing process for viscoelastic fluid flows obviously varied with time at relatively high Wi (*e.g.*, Wi > 5) in this microchannel. Chaotic flow motions were continuously induced in both the junction of three inlets and the rhombic structures, as shown in the supplementary videos 2 and video 3. The chaotic motions were firstly induced in the junction of three inlets. After that, in the straight channel, unlike the stratified status in Newtonian fluid case, the fluid flows of different concentration keep oscillating acting as the irregular wave of the main flow and the fluids keeps intertwining with each other and mixing with rolling together. When the flow evolves to the rhombic structures, the Newtonian fluid is equally separated into two shares at the beginning cusps of the rhombic structures. However, at the junctions the viscoelastic fluid flows separated randomly and non-uniformly as a result of unstable flow motions, with the high-concentration flow in the middle waving which disturbs the flow downstream and enhances the mixing process. In the rhombic structures, generally the high- or low-concentration fluid flow behaves in an irregular banding shape in the viscoelastic fluid flow. The transversal width of the flow pattern continuously changes with intertwining and rolling of different-concentration fluid. Finally, the concentration distribution becomes uniform rapidly because of the strong convection,

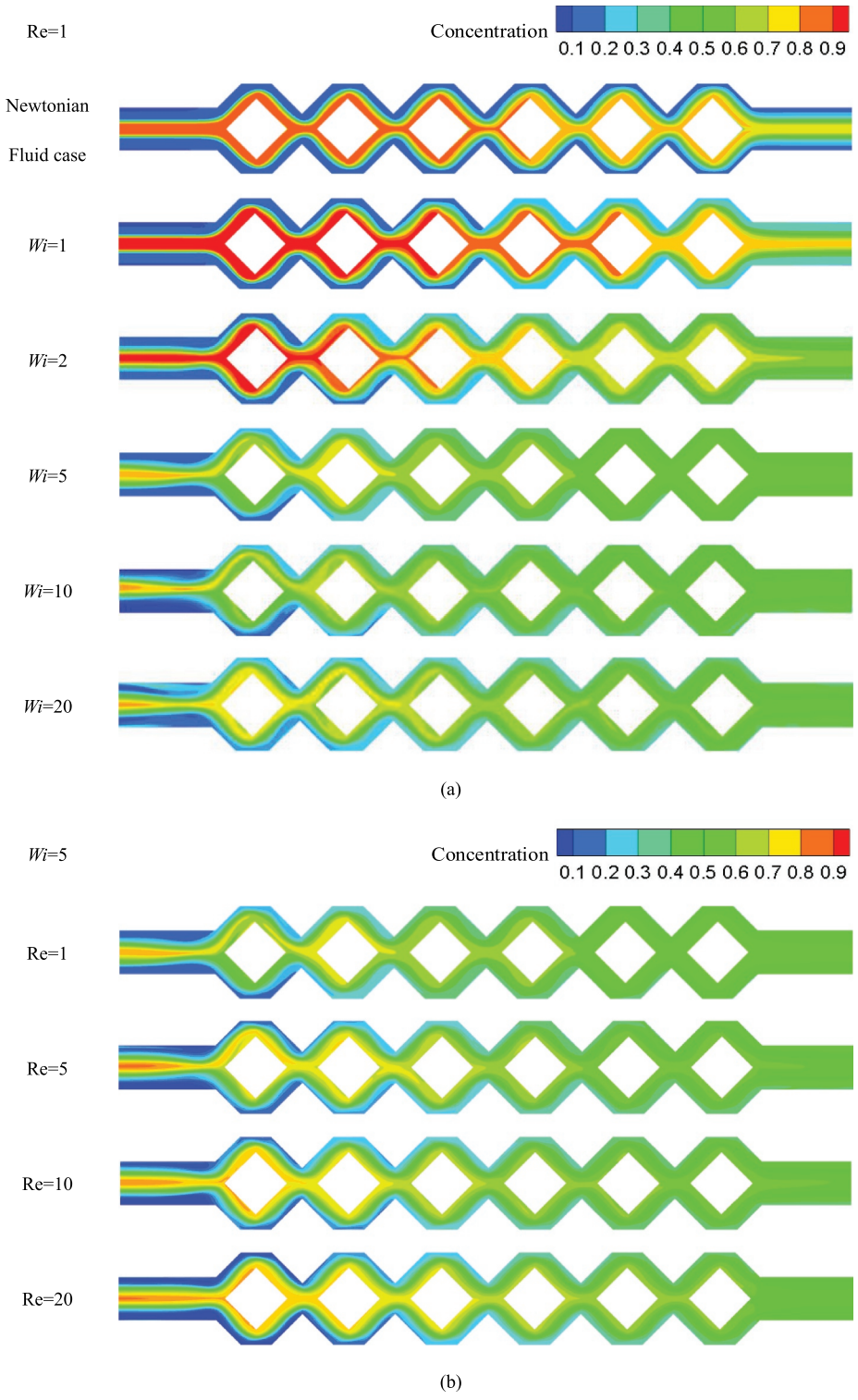

Fig. 7. Mixing performance of different working fluids under different conditions: (a) Time-averaged concentration distribution at different Wi; (b) distributions of time-averaged concentration contribution at different Re.

and a good mixing performance is achieved at the outlet.

Fig. 10 discusses the flow pattern in Newtonian fluid flow and viscoelastic fluid flow by comparing the streamlines of two typical cases, *i.e.*, Newtonian fluid flows at Re = 1 and viscoelastic fluid flows at Re = 1 and Wi = 20. In Newtonian fluid flow, which is laminar, the streamlines stay parallel to the flow direction without any normal-wise motion along the channel. Unlike the regular flow pattern in Newtonian fluid case, the streamlines in viscoelastic fluid flows twist in the middle of the channel, which increases the intersecting frequency of fluids with different concentrations. Moreover, the vortex structures are frequently generated from some specific positions near the inner wall of the rhombic channel and then undergo a process of expansion and contraction, inducing the flow swinging irregularly in the channel. Along with the swing motion, the fluids near the wall are coerced into the bulk, which mixes with the fluids in the bulk. In addition, near the rhombic wall the streamlines cross the channel at the intersection, and

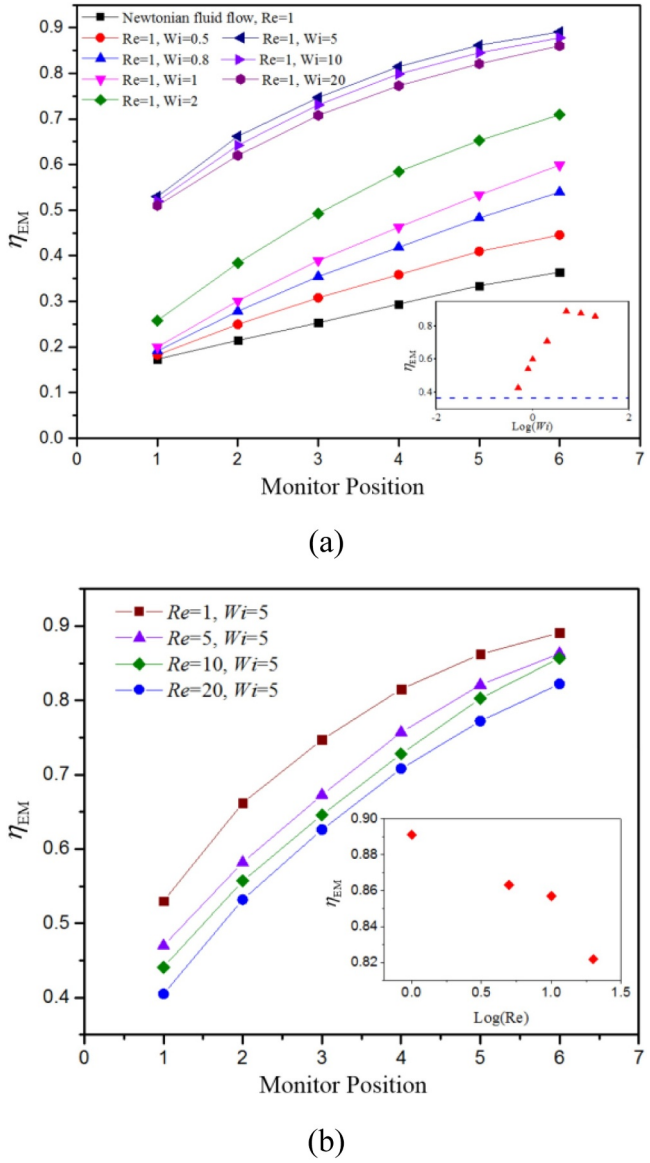

Fig. 8. Mixing efficiency η_{EM} for of Newtonian fluid and viscoelastic flows at 6 monitor lines under different flow conditions: (a) at different Wi; (b) at different Re.

swings up and down over time frequently at the junctions. Therefore, a rapid mixing in this case is finally motivated not only by strong convection in the respective channel but also by a frequent fluid exchanging near the channel junction. This explains the extraordinary mixing enhancement in viscoelastic fluid flow passing through this rhombic channel.

Fig. 11 identifies the convection effect on the mixing by showing the time-averaged convection term $<\mathbf{u}\cdot\nabla c>$ in Eq. (11). The term $<\mathbf{u}\cdot\nabla c>$ in Newtonian fluid case is too tiny to take into account. In contrast, it is significant in viscoelastic fluid flows especially in the bulk region and the first three rhombic structures of the channel where the interface between two fluids of different concentrations exist. This directly confirmed the significant convection contribution to the mixing enhancement in viscoelastic fluid flow.

4.3. Role of microstructures playing in the flow

The above analysis clearly shows the occurrence of elastic instabilities in the proposed micro-mixer, which is responsible for the mixing enhancement. It is then natural to see how the polymers embedded in the viscoelastic fluids act on the flow to induce the above unstable flow motions. It is known that the polymers' behavior is greatly influenced by the local flowtype. According to Astarita (1979) and Wagner (Wagner and McKinley, 2016) the flowtype parameter, ξ is defined as:

$$\xi = \frac{|\dot{\gamma}| - |\Omega|}{|\dot{\gamma}| + |\Omega|}$$

where $|\dot{\gamma}|=\sqrt{2\mathbf{D}:\mathbf{D}}$ and $|\Omega| = \sqrt{2\Omega:\Omega}$ are the magnitudes of deformation rate $\mathbf{D}$ and vorticity tensors Ω. The flowtype parameter varies between -1 and 1 that the values of -1 corresponds to purely rational flows, and the values of 0 corresponds to purely shearing flows and values of $+1$ corresponds to purely extensional flows. Fig. 12(a) shows the local flowtype parameter of rhombic microchannels. It is clear that the flowtype is dominated by extensional kinematics in the junctions of rhombic microchannels and shearing kinematics near the wall and the corners. Then, to understand the behavior of the polymers, we concentrate on the trace of conformation tensor ($\mathrm{tr}(\mathbf{C}) = C_{11} + C_{22} + C_{33}$), which represents the extension of polymers. Fig. 12(b) illustrates the distribution of time-averaged $\mathrm{tr}(\mathbf{C})$ for viscoelastic fluid flow under different conditions in the channel. In general, the extension of polymers ($\mathrm{tr}(\mathbf{C})$) increases with Wi at the same Re with a similar distribution of disordered filament-like structures especially near the wall and the corner where strong shear exists, and also in the junction of the rhombic-structure channels where strong extension exists. Moreover, the polymers are found to undergo a process of alternant stretching and rebounding along the flow direction, which is responsible for the occurrence of elastic instabilities in this channel.

After illustrating the polymers' behavior in the flow, we then make a further step to figure out how it influences on the flow stability. Unlike that in Newtonian fluids, the polymers are capable of storing energy during stretching by the main flow and also providing energy to the flow during its relaxation. In other words, an infinite fluid element in viscoelastic fluid flow contains both the kinetic energy and the elastic energy. Also, the alternating stretching and relaxation of polymers, which implies the role of the polymers changing during the flow, can act as a trigger of the flow instability. In this part, the additional energy exchange between the main flow and the polymers is taken into consideration. To this end, the energy budget for viscoelastic fluid flow was firstly derived according to Eqs. (2) and (3) to get the energy balance for the instantaneous kinetic energy E_k ($E_k = u_i u_i/2$,), the instantaneous elastic energy E_p ($E_p = \mathrm{tr}(\mathbf{C})/2$) and the time-averaged turbulent kinetic energy E_{kf} ($E_{kf} = \langle u'_i u'_i \rangle/2$), respectively, as follows:

$$\frac{\partial E_k}{\partial t} + u_j\frac{\partial E_k}{\partial x_j} = -\frac{\partial}{\partial x_k}\left(\frac{pu_i}{\rho} - \underbrace{\frac{\upsilon\partial E_k}{\partial x_k}}_{D_K} - \frac{u_i\tau_{p,ik}}{\rho}\right) - \underbrace{\upsilon\left(\frac{\partial u_i}{\partial x_k}\frac{\partial u_i}{\partial x_k}\right)}_{\varepsilon_\upsilon} - \underbrace{\tau_{p,ik}\frac{\partial u_i}{\rho\partial x_k}}_{G_p} + \underbrace{f_i u_i}_{F_k} \tag{12}$$

$$\frac{\partial E_p}{\partial t} + u_j\frac{\partial E_p}{\partial x_j} = \underbrace{C_{ik}\frac{\partial u_i}{\rho\partial x_k}}_{G_p} - \underbrace{\frac{tr(\mathbf{C}) - 3}{2\lambda}}_{\varepsilon_p} \tag{13}$$

$$\frac{\partial E_{kf}}{\partial t} + u_j\frac{\partial E_{kf}}{\partial x_j} = \underbrace{-\langle u'_i u'_k\rangle\frac{\partial\langle u_i\rangle}{\partial x_k}}_{P'_K} + \frac{\partial}{\partial x_k}\left(\frac{\langle p'u'_i\rangle}{\rho}\delta_{ik} - \upsilon\frac{\partial E_{kf}}{\partial x_k} + \underbrace{<u'_i u'_i u'_k>}_{D'_K} - \frac{\langle\tau'_{p,ik}u'_i\rangle}{\rho}\right)$$
$$- \underbrace{\upsilon\left\langle\frac{\partial u'_i}{\partial x_k}\frac{\partial u'_i}{\partial x_k}\right\rangle}_{\varepsilon'_\upsilon} - \underbrace{\left\langle(\tau_{p,ik})'\frac{\partial u'_i}{\rho\partial x_k}\right\rangle}_{G'_p} \tag{14}$$

where $\langle\cdot\rangle$ indicates the time-averaged variables; F_k is the energy input by the external force; D_k is the generalized diffusion term of the instantaneous kinetic energy; G_p is the energy exchange between the flow motion and the polymers: $G_p > 0$ indicates the energy absorption from the flow structures into the polymers, otherwise, the energy release

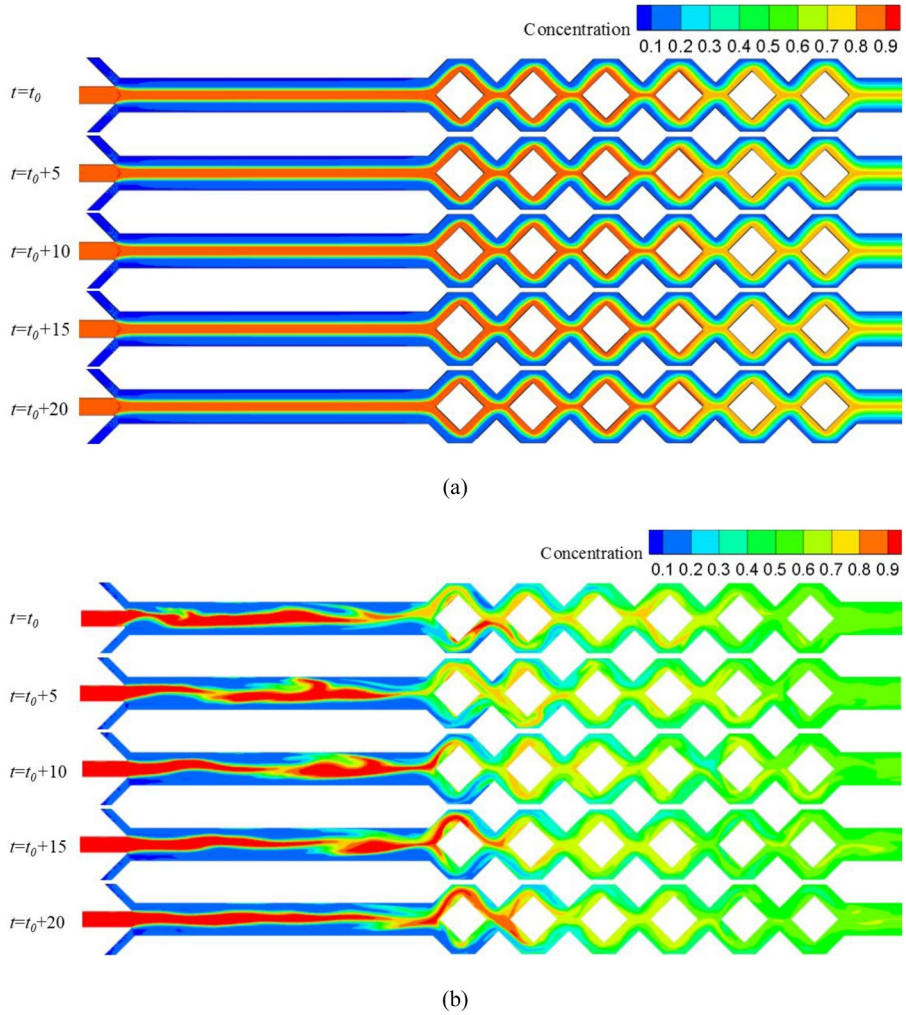

Fig. 9. Temporal evolution of concentration field for (a) Newtonian fluid flows at Re = 1 and (b) viscoelastic fluid flows at Re = 1, Wi = 20. t_0 is an instant of the calculation results, and t_0 = 500 in this case and in Fig. 10.

from the polymers to the flow; ε_v is the viscous dissipation of the mean kinetic energy E_k; P'_K is the energy exchange between the mean flow and the turbulent fluctuations by Reynolds stress; ε'_v is the viscous dissipation of the turbulent kinetic energy E_{kf}; D'_K is the generalized diffusion term of the turbulent kinetic energy; G'_p is the elastic contribution to the turbulent fluctuations: $G'_p > 0$ indicating the elastic dissipation of the turbulent fluctuations, otherwise, the energy supply from the polymers to the turbulent fluctuations. The following analysis mainly focuses on the elasticity contributed terms G_p and G'_p which show the role of polymers.

Fig. 13 shows the distributions of $\langle G_p \rangle$ and $-\langle G'_p \rangle$ in this rhombic channel. It is seen that $\langle G_p \rangle$ is mostly positive, *i.e.*, the polymers absorbs energy from the main flow. As mentioned before, the polymers undergo a process of alternant stretching and rebounding along the flow direction. With the change of the polymers' behaviors in this specially designed channel, their role also changes. As shown in Fig. 13(a), in some parts of the channel, such as the rear of the bends and the junctions, the polymers release energy to the main flow with negative $\langle G_p \rangle$ which is responsible for the occurrence of the unstable flow motions. As for the distribution of $-\langle G'_p \rangle$, it is mostly positive indicating the polymers supply energy to the fluctuations instead of dissipating the fluctuations. The maximum of $-\langle G'_p \rangle$ locates in the turnings and the intersections where the polymers are severely deformed due to the local strong shear and extension. Combining with the streamlines in Fig. 11, it is observed that the vortex structures tend to lie in the region of high $-\langle G'_p \rangle$ which is in striation and parallel to the channel. This also implies the role of the polymers in the generation and the maintenance of vortex structures. Moreover, when the vortex structures are comparable with the main flow, the main flow squeezed them to the wall, and when the vortex structures accumulate enough energy, they are then forced to the bulk. These competing processes appear alternatively and dominate the flow to reach a final balance. Therefore, on the one hand, the main flow firstly stretches and supplies energy to the polymers; on the other hand, the polymers maintain or enlarge the vortex structures from decaying to be laminar. In sum, we can attribute the observed unstable flow motions to the flexibility of polymers together with this special geometry owning the junctions and the corners, which changed the polymers' role on the flow.

5. Conclusions

In this work, an efficient micro-mixer by elastic instabilities and turbulence of viscoelastic fluids has been designed and investigated through both experimental visualization and numerical simulation. From the experimental aspect, the mixing processes of Newtonian fluid flow and viscoelastic fluid flow were visualized in the proposed micro-mixer via the solution with green fluorescent particles. A remarkable mixing enhancement was observed for the viscoelastic fluid flow because of unstable flow motions occurring therein. Also, with the biocompatible working fluids, the efficient mixing in the designed micro-mixer has great potential to be applied in bioengineering and chemical engineering. To achieve an in-depth understanding of mixing process,

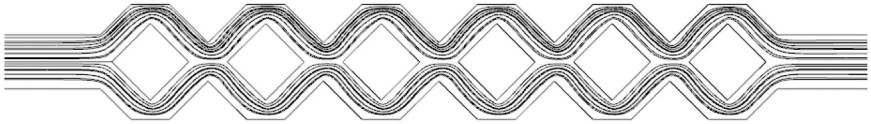

(a) Newtonian fluid flow at Re=1

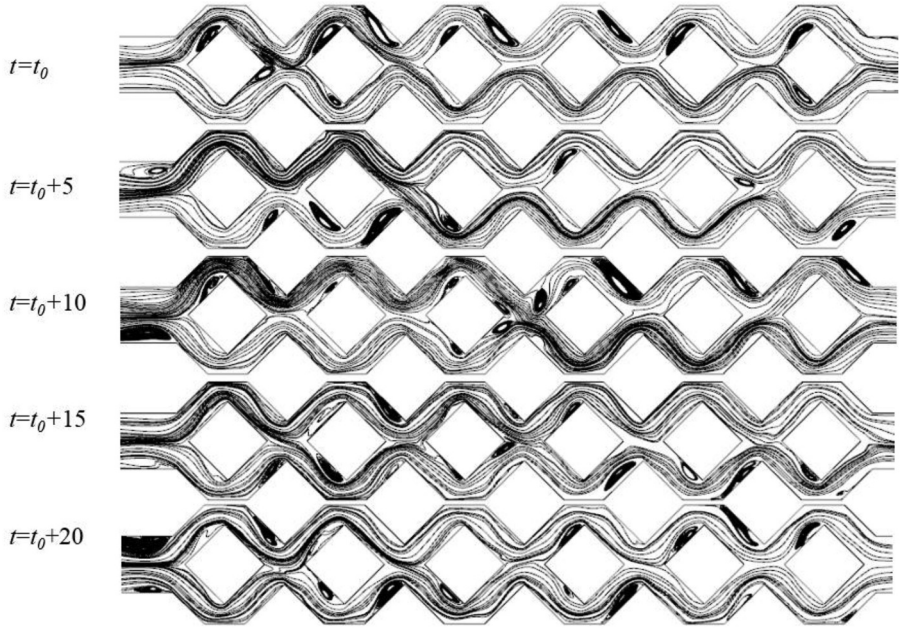

(b) viscoelastic fluid flows at Re=1 and *Wi*=20.

Fig. 10. Streamlines of (a) Newtonian fluid flows at Re = 1 and (b) viscoelastic fluid flows at Re = 1 and Wi = 20.

numerical simulations of both Newtonian fluid flow and viscoelastic fluid flow were carried out as a compensation. From the numerical aspect, the visualization of the mixing process and the quantification of the mixing efficiency show an obvious mixing enhancement in viscoelastic fluid flow similar to that observed in the experiments. After that, mechanistic analysis on the mixing enhancement was conducted by analyzing the flow patterns and the role of convection, which ascribes the mixing enhancement to the unstable flow motions and its consequent convection effect. Finally, the behaviors and the role of polymers acting on the flow are investigated to shed some light on the occurrence of flow instabilities. From the instantaneous viewpoint, the polymers do not only absorb energy from the main flow but also release energy to the main flow in some parts of this special designed channel; from the fluctuating viewpoint, the energy release from the polymers is the key to maintain the fluctuations of the unstable flow motions.

It is worth noting that the present work mainly evaluated the mixing performance by elastic instabilities and figuring out the mechanisms for the mixing enhancement. However, as an efficient micro-mixer, besides the mixing efficiency, we also need to take into account of the energy consumption, the output and the fabrication cost, which needs to be

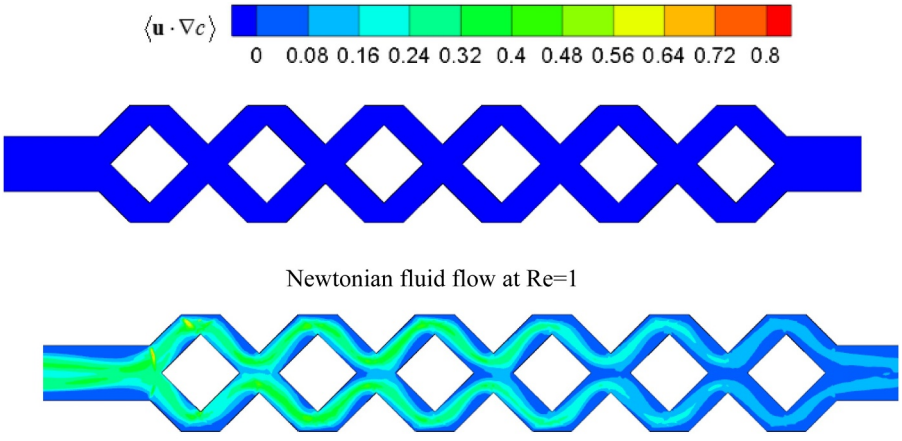

Newtonian fluid flow at Re=1

Viscoelastic fluid flow at Re=1, *Wi*=20

Fig. 11. Comparison of the distribution of $\langle \mathbf{u} \cdot \nabla c \rangle$ between Newtonian fluid flow at Re = 1 and viscoelastic fluid flow at Re = 1, and Wi = 20.

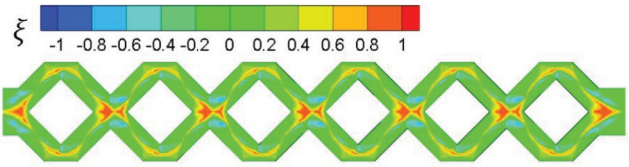

a) Time-averaged local flowtype parameter of the viscoelastic flow at Re=1, and Wi=20

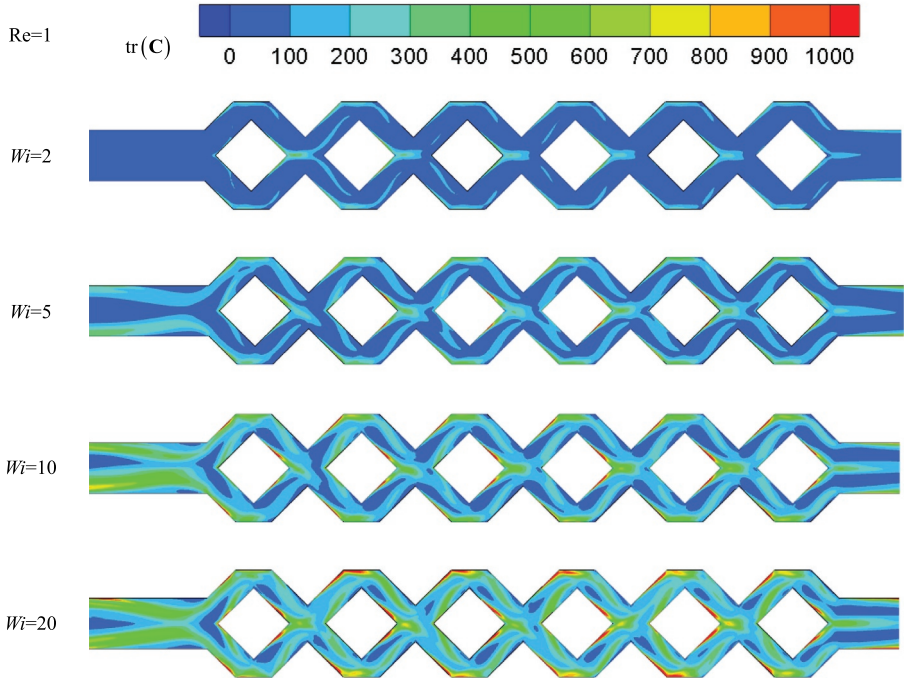

b) Distributions of time-averaged tr(**C**) for viscoelastic fluid flows at different *Wi*

Fig. 12. Distributions of time-averaged tr(**C**) for viscoelastic fluid flows at different Wi.

considered in our future work. For example, increasing the number of the rhombic structures improves the mixing performance, while brings in the additional drag resistance or the energy consumption. Moreover, the mixing performance saturates after a few rhombic structures, indicating the existence of an optimal number of the rhombic structures under different conditions. Therefore, the scaling between the mixing efficiency, the drag resistance, Re, Wi, as well as the number of the rhombic structures is necessary to guide the application of this type of micromixer.

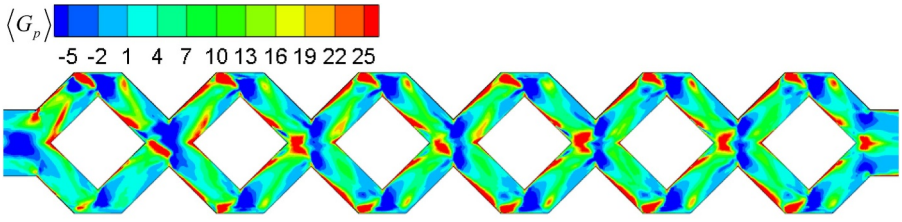

(a)

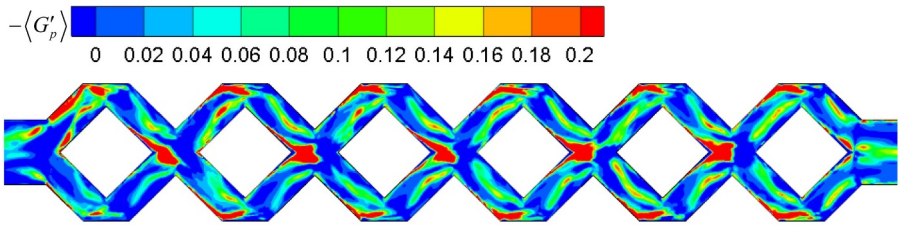

(b)

Fig. 13. Distributions of time-averaged energy transfer between the flow motion and microstructures from the mean and fluctuating viewpoints: (a) $\langle G_p \rangle$ and (b) $-\langle G'_p \rangle$.

Acknowledgments

The authors thank the National Natural Science Foundation of China (51576051, 51506037, 51606054), the Fundamental Research Funds for the Central Universities (HIT.NSRIF.201667).

Supplementary materials

Supplementary material associated with this article can be found, in the online version, at doi:10.1016/j.ijheatfluidflow.2018.09.006.

References

Affanni, A., Chiorboli, G., 2010. Chem 147, 748.
Akgönül, S, Özbey, A, Karimzadehkhouei, M, et al., 2017. Microfluid. Nanofluid 21 (7), 118.
Ammar, H, el Moctar, AO, Garnier, B, et al., 2014. ASME J. Fluids Eng. 136 (12), 121101.
Arratia, P.E., Thomas, C.C., Diorio, J., Gollub, J.P., 2006. Phys. Rev. Lett. 96, 144502.
Astarita, G., 1979. J. Non-Newton Fluid 6, 69–76.
Bhagat, A.A.S., Dagani, G., Peterson, E.T., Lee, J.H, Papautsky, I., 2005. In: MOEMS-MEMS Micro & Nanofabrication, International Society for Optics and Photonics, pp. 291–297 January.
Bonn, D., Ingremeau, F., Amarouchene, Y., Kellay, H., 2011. Phys. Rev. E 84, 045301.
Burghelea, T., Segre, E., Bar-Joseph, I., Groisman, A., Steinberg, V., 2004. Phys. Rev. E 69, 066305.
Burghelea, T., Segre, E., Steinberg, V., 2007. Phys. Fluids 19, 053104.
Chen, X, Li, T, 2017. Chem. Eng. J. 313, 1406–1414.
Chen, X, Zhao, Z, 2017. Analytica Chimica Acta 964, 142–149.
Chung, C.K., Shih, T.R., 2008. Microfluid. Nanofluid 4, 419.
Engler, M., Föll, C., Kockmann, N., Woias, P., 2003. In: Proceedings of the 11th European Conference on Mixing. 277284.
Fattal, R., Kupferman, R., 2004. J. Non-Newtonian Fluid Mech 123, 281.
Favero, J.L., Secchi, A.R., Cardozo, N.S.M., Jasak, H., 2010. J Non-Newtonian Fluid mech 165, 1625.
Feng-Chen, L., Hong-Na, Z., Yang, C., Tomoaki, K., Haruyuki, K., Marie, O., 2012b. Chin. Phys. Lett. 29, 094704.
Galindo-Rosales, F.J., Alves, M.A., Oliveira, M.S.N, 2013. Microfluid. Nanofluid 14, 1.
Gan, H.Y, Lam, Y.C., Nguyen, N.T., Tam, K.C., Yang, C., 2007a. Microfluid. Nanofluid 3, 101.
Gan, H.Y., Lam, Y.C., Nguyen, N.T., Tam, K.C., Yang, C., 2007b. Microfluid. Nanofluid 3, 101.
Gan, H.Y., Lam, Y.C., Nguyen, N.T., 2006. Appl. Phys. Lett. 88, 224103.
Groisman, A., Steinber, V., 2001. Nature 401, 905.
Groisman, A., Steinberg, V., 2000. Nature 405, 53.
Groisman, A., Steinberg, V., 2004. J. New Phys. 6, 29.
Habla, F., Tan, M.W., Haßlberger, J., Hinrichsen, O., 2014. J. Non-Newtonian Fluid Mech. 212, 47.
Haward, S.J., Poole, R.J., Alves, M.A., et al., 2016a. Phy. Rev. E 93 (3), 031101.
Haward, S.J., 2016. Biomicrofluidics 10, 043401.
Haward, S.J., McKinley, G.H., Shen, A.Q., 2016b. Sci. Reports 6.
Haward, S.J., Ober, T.J., Oliveira, M.S., Alves, M.A., McKinley, G.H., 2012. Soft Matter 8, 536.
Hong, S.O., Cooper-White, J.J., Kim, J.M., 2016. Appl. Phys. Lett. 108, 014103.
Julius, L.A.N., Jagannadh, V.K., Michael, I.J., Srinivasan, R., Gorthi, S.S., 2016. J. BioChip 10, 16.
Jun, Y., Steinberg, V., 2011. Phys. Rev. E 84, 056325.
Kockmann, N., Woias, P., 2003. Micromachining and Microfabrication. International Society for Optics and Photonics, pp. 319.
Lam, Y.C., Gan, H.Y., Nguyen, N.T., Lie, H., 2009. Biomicrofluidics 3, 014106.
Li, D.-Y., Li, X.-B., Zhang, H.-N., Li, F.-C., Qian, S.Z., Joo, S.W., 2016a. Exp. Therm. Fluid Sci. 77, 226.
Li, D.–Y., Zhang, H.–N., Cheng, J.-P., Li, X.–B., Li, F.–C., Qian, S., Joo, S.W., 2017. Microfluid Nanofluid 21, 25.
Li, F.-C., Kinoshita, H., Li, X.-B., Oish, M., Fujii, T., Oshima, M., 2010. Exp. Therm. Fluid Sci. 34, 20.
Li, X.-B., Zhang, H.-N., Cao, Y., Oshima, M., Li, F.-C., 2014. Advances Mech. Eng. 6, 734175.
Li, X.-B., Oishi, M., Matsuo, T., Oshima, M., Li, F.-C., 2016b. ASME J. Fluid Eng. 138, 091401.
Li, Z., Kim, S.J., 2017. Chem. Eng. J. 313, 1364–1369.
McGovern, M.E., Buttlar, W., Reis, H.J., 2018. Nondestruct. Eval. Diagn. Progn. Eng. Syst. 1 (1), 011002.
Mengeaud, V., Josserand, J., Girault, H.H., 2002. Analytical Chem. 74, 4279.
Mouheb, N.A., Malsch, D., Montillet, A., et al., 2012. Chem. Eng. Sci. 68 (1), 278–289.
Ng, T.N., Chen, X.Q., Yeung, K.L., 2015. RSC Adv. 5 (18), 13331–13340.
Ottino, J.M., Wiggins, S., 2004. Philos. Trans.: Math. Phys. Eng. Sci. 923.
Pan, L., Morozov, A., Wagner, C., Wagner, C., Arratia, P.E., 2013. Phys. Rev. Lett. 110, 174502.
Pathak, J.A., Ros, D., Migler, K.B., 2004. Phys. Fluids 16, 4028.
Poole, R.J., Alves, M.A., Oliveira, P.J., 2007. Phys. Rev. Lett. 99, 164503.
Soulages, J., Oliveira, M.S.N., Sousa, P.C., Alves, M.A., McKinley, G.H., 2009. J. Non-Newton. Fluid Mech. 163, 9.
Squires, T.M., Quake, S.R., 2005. Rev. Mod. Phys. 77, 977.
Stroock, A.D., Dertinger, S.K., Ajdari, A., Mezić, I., Stone, H.A., Whitesides, G.M., 2002. Science 295, 647.
Ta, BQ, Le Thanh, H, Dong, T, et al., 2015. J. Micromech. Microeng. 25 (9), 094004.
Wagner, C.E., McKinley, G.H., 2016. J. Non-Newton Fluid 233, 133–145.
Zhang, H.-N., Li, F.-C., Cao, Y., Tomoaki, K., Bo, Y., 2013. Chin. Phys. B 22, 024703.
Zhang, H.-N., Li, F.-C., Li, X.-B., Li, D.-Y., Cai, W.–H., Yu, B., 2016. Chin. Phys. B 25, 094701.
Zhang, H.–N., Li, D.-Y, Li, X.–B., Cai, W.-H, Li, F.-C, 2017. ASME J. Fluids Eng. 139 (9).